Chapter 3

Bulk Properties

3.1 Introduction

A surface is directly connected to the underlying bulk, which means that the properties of the bulk material will most probably influence the properties and behavior of the surface. This chapter is therefore devoted to the investigation of different bulk structures, in order to study their equilibrium atomic structure, relative stability, electronic and magnetic properties. The results are then used to obtain the surface energy and formation energy of films at the surface. Additionally, it is the basis for comparing the theoretical results with experimental data.

The starting point of any investigation is the determination of the theoretical lattice parameter. Thermodynamic properties will be important as well for the following discussion of the surfaces.

To obtain the equilibrium bulk structure, the total energy is minimized with respect to the unit cell volume. The lattice parameters and bulk modulus are determined by fitting a set of data points to the Murnaghan equation of state, [54]:

$$E(V) = E(V_0) + \frac{B_0}{B_0^{'}} \left[\frac{V_0 \ (V_0/V)^{B_0^{'}-1}}{B_0^{'}-1} + V(1 - \frac{(V_0/V)}{B_0^{'}-1}) \right] \quad , \tag{3.1}$$

where V_0 is the equilibrium volume at zero temperature, $E(V_0)$ is the minimum energy of the system, B_0 is the bulk modulus, defined as

$$B_0(T,p) = -V \frac{\partial p}{\partial V} |_T \quad , \tag{3.2}$$

and $B_0^{'}$ is the pressure derivative of bulk modulus at $p = 0$ and constant temperature:

$$B_0' = -\frac{\partial}{\partial p}\,(V \frac{\partial p(T,V)}{\partial V})_{T,p=0} \qquad . \tag{3.3}$$

The cohesive energy is always defined as the energy needed to form a crystal from the individual free atoms [1] which form the crystal. For example, the cohesive energy for MnSi is obtained as:

$$E_{\rm coh} = E_{\rm tot}^{\rm MnSi-bulk} - E_{\rm tot}^{\rm Mn-atom} - E_{\rm tot}^{\rm Si-atom} \qquad . \tag{3.4}$$

where $E_{\rm tot}^{\rm MnSi-bulk}$, $E_{\rm tot}^{\rm Mn-atom}$ and $E_{\rm tot}^{\rm Si-atom}$ are the total energies of MnSi bulk, Mn and Si free atoms.

The energy difference between a crystal and it's constituent parts as solid phases is called the formation enthalpy of the solid at zero temperature, which is given by:

$$\Delta H({\rm MnSi}) = E_{\rm tot}^{\rm MnSi-bulk} - E_{\rm tot}^{\rm Mn-bulk} - E_{\rm tot}^{\rm Si-bulk} \qquad . \tag{3.5}$$

where $E_{\rm tot}^{\rm MnSi-bulk}$, $E_{\rm tot}^{\rm Mn-bulk}$ and $E_{\rm tot}^{\rm Si-bulk}$ are the total energies of the bulk phases of MnSi, Mn and Si, respectively.

The first-principles calculations are performed using density-functional theory (DFT). For non-magnetic cases the exchange-correlation functional is treated with the local-density approximation (LDA) [55]. In the spinpolarized calculations, the generalized gradient approximation in the parameterization of Perdew, Burke, and Ernzerhof (GGA-PBE 96) [34] for the exchange-correlation potential, is used [2]. It has been demonstrated and confirmed by test calculations that GGA gives a much better description for bulk Mn than the local-spin-density approximation (LSDA). The Kohn-Sham equations were solved applying the full-potential augmented plane wave plus local orbital (FP-APW + lo) method [37].

This chapter presents ab initio total energy calculations of Si, Mn, MnSi. The effects of pressure on structure, bonding and electronic structures are also discussed.

[1] The total energy for a spin-polarized free atom is calculated. Due to the periodic boundary conditions the self-consistent calculations for the atom are performed using a large cubic supercell, so that interactions between the atoms are negligible.

[2] The convergence test are presented in Appendix A.

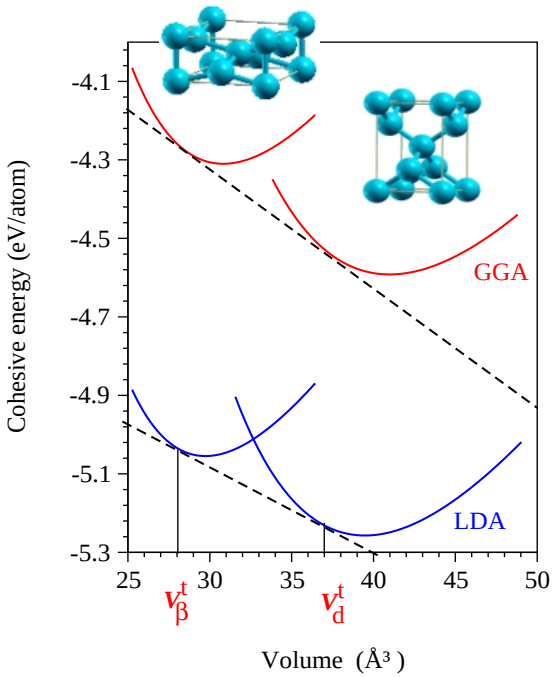

Fig. 3.1: Energy-volume curve for bulk diamond and β-tin Si using GGA (red line) and LDA (blue line) functionals. The dashed lines are the common tangents, the slope of the common tangents is the pressure for the phase transition from the diamond to the β-tin structure.

3.2 Bulk Silicon

3.2.1 Structural Properties and Thermodynamical Stability

Silicon with the atomic number 14 belongs to the group-IV elements in the periodic table. It has 4 unpaired electrons in the outer shell which leads to the formation of 4 bonds with neighboring atoms in the diamond structure of the Si-bulk phase. The conventional cell of Si-bulk is a fcc lattice type with two basis atoms at (0 , 0 , 0) and $(\frac{1}{4}, \frac{1}{4}, \frac{1}{4})$. The primitive lattice vectors are $\mathbf{a_1} = \frac{a}{2}\hat{\mathbf{i}} + \frac{a}{2}\hat{\mathbf{k}}$, $\mathbf{a_2} = \frac{a}{2}\hat{\mathbf{i}} + \frac{a}{2}\hat{\mathbf{j}}$ and $\mathbf{a_3} = \frac{a}{2}\hat{\mathbf{j}} + \frac{a}{2}\hat{\mathbf{k}}$, where $\hat{\mathbf{i}}$, $\hat{\mathbf{j}}$, $\hat{\mathbf{k}}$ are the unitary vectors along the x , y , z directions, respectively. There is a structural phase transition from four-fold-coordinated diamond structure to a tetragonal six-fold-coordinated β-tin phase at pressure of 99 GPa [56]. The β-tin has a bcc lattice with atoms at (0, 0, 0) and $(\frac{1}{2}, 0, \frac{3}{4})$ positions.

To obtain the lattice parameter, a sequence of calculations are performed for bulk Si in both diamond and β-tin phases in nine separate calculations for volumes varying between -20 % and +20 % of the experimental volume. The volume corresponding to the minimum energy identifies the equilibrium lattice parameter, a_0. The cohesive energy versus volume curves calculated with GGA and LDA functional for

both diamond and β-tin are shown in Fig. 3.1. The blue curves are LDA and the red curves are GGA results, the dashed lines are common-tangents, the slope of these lines indicate the phase transition pressure.

For the diamond structure, the LDA calculations show the well-known overbinding effect value with a cohesive energy overestimated by +11.4% and lattice parameter underestimated by -0.37 %, as compared to the experimental results.

In GGA, on the other hand, the equilibrium volume is overestimated by 0.74 % and the cohesive energy, E_{coh}, is underestimated by -0.86 % . Here, we do not consider the zero point vibrations of lattice. Therefore, the calculated lattice constant in this work is smaller than that, including zero point vibrations. The order of magnitude of the zero point vibrations can be estimated from the uncertainty relation [57]. Taking into account the zero point vibrations increase the lattice constant up to 0.5%. Our results are compared to GGA-PW 91 functional [58] and experimental data in Tab. 3.1. The lattice parameter (a_0), bulk modulus (B_0), and derivative of bulk modulus, B_0' calculated using LDA are in good agreement with the experimental results. The difference in the GGA-PBE 96 and GGA-PW 91 results are just a few percent.

The pressure of the phase transition is obtained via the Gibbs common tangents construction using the energy versus volume plot for the two phases, i.e.,

$$p_t = -\frac{E_t^d - E_t^\beta}{V_t^d - V_t^\beta} \quad , \tag{3.6}$$

where P_t is phase transition pressure, E_t^d and E_t^β are energy at the transition for diamond and β-tin structures, V_t^d and V_t^β are the transition volume for the mentioned structures.

In the prediction of the transition pressure, the LDA results are significantly lower than the experimental value, whereas the GGA increases the transition pressure, leading to a value that is close to the experimental value. The transition pressure is a sensitive quantity, since it depends not only on the energy but also on its first derivative with respect to the volume. The pressures calculated with both GGA PBE / PW functional are 4 % - 5 % smaller than the experimental value while this is 22 % smaller for LDA.

3.2.2 Electronic Properties

The diamond structure of silicon is found to be the ground state structure at zero pressure and temperature, therefore only the electronic properties of this structure

Table 3.1: Comparison of the calculated lattice constant (a_0), bulk modulus (B_0), pressure derivative of the bulk modulus ($B_0^{'}$), and cohesive energy ($E_{\rm coh}$) for Si diamond and β-tin structures using LDA, GGA-PBE and GGA-PW. The transition presure between the two phases, as well as their volumes V_t^d and V_t^β at the transition point are given . The experimental values are taken from Ref. [3] and [4] and for the GGA-PW values the results of Moll et al [5].

		LDA	GGA PBE	GGA PW	EXP.
Diamond					
	a_0(Å)	5.41	5.47	5.59	5.43
	B_0(GPa)	94.9	87.8	85.2	98.8
	B_0'	4.25	4.25	3.70	4.09
	$E_{\rm coh}$(eV / atom)	5.26	4.59	4.64	4.63
β-tin					
	a_0(Å)	4.73	4.78	4.82	—
	B_0(GPa)	115	106	106	—
	B_0'	4.89	4.25	4.10	—
	$E_{\rm coh}$(eV / atom)	5.06	4.31	—	4.63
	c/a	0.55	0.55	0.551	0.552
	$V_t^d/V_0^d(exp.)$	0.926	0.937	0.928	0.918
	$V_t^\beta/V_0^d(exp.)$	0.703	0.715	0.706	0.710
	p_t (GPa)	70	95	106	99-101

will be discussed in the following. It can be seen from the band structure that silicon (in the diamond structure) is semiconductor. It has an indirect band gap of 1.17 eV [3].

The band gap calculated with DFT-LDA (GGA), which is determined by the energy difference between the top of highest occupied state (valence band) and bottom of lowest unoccupied state (conduction band), is almost half of the value of the experimental band gap. Having a value of 0.5 eV for the calculated band gap, agrees poorly with the experimentally observed band gap. The calculated band structure and density of states for both the LDA and GGA functionals at their equilibrium volume are shown in Fig. 3.2. The GGA and the LDA bandstructures are quite similar, but the conduction and the upper valence bands in LDA are shifted by 0.2 eV with respect to their GGA counterparts.

The electron density of states (DOS) is shown in Fig. 3.2. Three energy regions for the valence bands can be distinguished: the s band's contribution is found in the range between -12 eV and -8 eV below the Fermi level; a hybridization of s and p

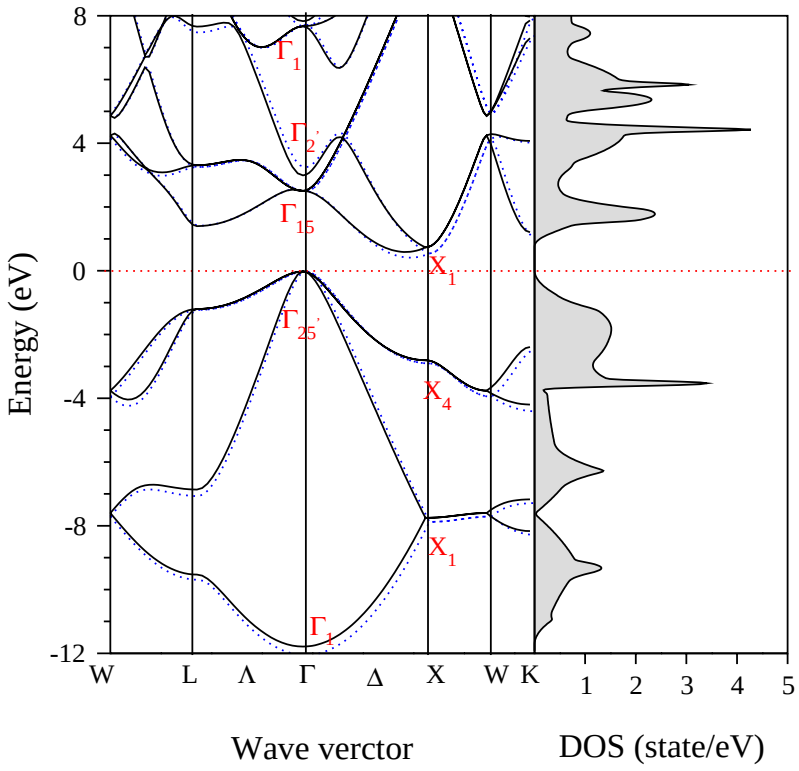

Fig. 3.2: Band structure and DOS plot for bulk Si at equilibrium volume with a $(10\times10\times10)$ k-point grid in the Brillouin-Zone using GGA (solid lines) and LDA (dash lines) functionals. The energy zero is taken to be the top of the valence band.

bands is found between -4 eV and -8 eV below the Fermi level; while p bands are observed between zero to -4 eV below Fermi level.

It is known from photoemission experiments, that the top of the valence band is located at k=0, denoted $\Gamma_{25}\prime$ [61]. The minimum of the conduction band is found close to the X point (k=$(2\pi/a)(\frac{1}{2},0,0)$) along the Δ symmetry line and has p-like character, cf. Fig. 3.2. The experimental optical gaps found at Γ and X points, respectively, are 3.4 eV and 4.4 eV, which is 1.0 eV and 0.9 eV higher than the values found in the present work. On the other hand, for deeper lying valence bands, the calculated band structure is in good agreement with the experiment, the relative error being less than 2 %. In Tab. 3.2.2 one can compare the eigenvalues of Kohn-Sham equations for Si bulk with photoemission measurement energy for some critical points in the Si-band structure. These value are calculated at theoretical lattice parameter. As one expects, the LDA results are closer to experimental observations.

Table 3.2: Electronic energies of Kohn-Sham equation for Si bulk.

	Γ_{1v}	$\Gamma_{25'v}$	Γ_{15c}	$\Gamma_{2'c}$	Γ_{1c}	X_{4v}	X_{1c}
LDA	-12.1	0.0	2.3	3.2	7.7	-3.1	0.6
GGA	-12.0	-0.2	2.5	2.8	7.5	-3.0	0.55
EXP	-12.5 [a]	0.0 [a]	3.4 [a]	4.15 [b]	7.6 [b]	-2.9 [a]	1.13 [a]

(a) Ref. [59]
(b) Ref. [60]

3.3 Bulk Manganese

Manganese (Mn) is one of the interesting and complex case in the metallic elements. According to Hund's rule, the magnetic moment of the free atom is as large as 5 μ_B which is the highest magnetic moment among transition metal elements. The stable phase under normal temperature and pressure condition is α-manganese (space group T_d^3—$I\bar{4}3m$) [62], which has complex cubic structure with 29 atoms per unit cell and shows non-collinear magnetism.

The Mn atoms in the α phase have magnetic moments between 0 and more than 3 μ_B [63]. The α-Mn phase undergoes a phase transition from antiferromagnetic (AFM) to non-magnetic (NM) at a Neél temperature of T_N = 95 K. This magnetic transition is coupled to a tetragonal crystal structure for the non-magnetic phase.

In the temperature interval from 1000 K to 1368 K the β phase will form. It has a cubic structure with twenty atoms per unit cell, the space group $P4_132$ [64] and a small magnetic moment [65, 66] . The fcc-γ phase exists in the temperature region from 1368 K to 1406 K and has an antiferromagnetic low-spin ground state. For high temperatures up to the melting point (1517 K) the non-magnetic bcc-δ structure is found. Under compression a phase transition to the antiferromagnetic hexagonal ϵ-structure [63] occurs.

3.3.1 Structural Properties

The calculations which are performed in this part are for fcc-γ structures with different magnetic ordering (PM, FM, AFM). The AFM ordering is considered as planes in (100) direction containing parallel magnetic moments ($i.e.$ in-plane FM). Extensive convergence test showed that an energy cutoff of 16 Ry and $(15 \times 15 \times 15)$ k-points in the Brillouin zone are sufficient to describe this structure. In order to

do calculation for AFM phase, a body-centered-tetragonal structure with lattice parameters, $a = b = \sqrt{2}\, c$ and $c = a_{fcc}$ is considered.

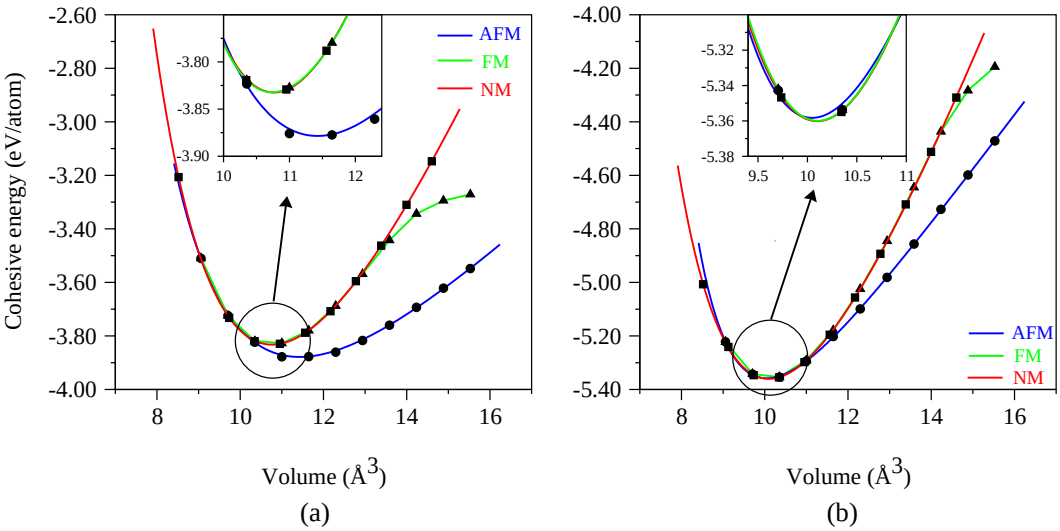

Fig. 3.3: The plot of total energy per atom versus unit cell volume, (E-V), with GGA (a) and LSDA (b). the circles, squares and triangle were used for antiferromagnetic, ferromagnetic and non-magnetic, respectively. The AFM ordering has lowest energy at equilibrium volume in GGA. The magnetovolume effect is not significant with LSDA. Magnetic and non-magnetic calculation have nearly the same E-V curve

In Fig. 3.3 the total energy is given as a function of volume for both GGA and LSDA functionals. The antiferromagnetic fcc-γ phase structure is energetically the ground state for GGA calculations. The lattice constant is 4% smaller than the α-Mn and the cohesive energy is lower than non-magnetic state by at least 50 meV. In the LSDA all calculations converge to a non-magnetic ground state at a volume interval in $\pm$10 % around equilibrium volume. GGA, on the other hand, predicts an increased equilibrium volume. This means a smaller deviation of the theoretical lattice parameter from the experimental result in GGA, compared to LSDA. In addition, LSDA increases the magnetovolume effect: an antiferromagnetic solution exists for expanded volume which is about 11 Å^3 while the AFM order found at volume around at 10 Å^3, for GGA.

The results for the cohesive energy, lattice constant and bulk modulus for the non-magnetic, ferromagnetic and antiferromagnetic ordering are summarized in Table 3.3 for GGA, LSDA and the experimental results. Some prominent details in this comparison that should be emphasized are:

(I) Use of different exchange-correlation functionals has a stronger influence on the total energy and equilibrium volume, than the magnetovolume effect.

(II) The difference between LSDA and GGA results for the magnetic cases are more

Table 3.3: Comparison of the cohesive energy E_{coh}, the lattice parameter a_0 and the bulk modulus B_0 of different magnetic ordering of manganese in fcc-γ structure.

fcc-γ structure	Magnetic Phase	E_{coh} (eV / atom)	a_0 (Å / atom)	B_0 (Mbar)
Present work (GGA)	AFM	3.87	3.59	1.35
	FM	3.82	3.47	2.76
	NM	3.83	3.50	2.72
Present work (LSDA)	AFM	5.36	3.42	3.07
	FM	5.38	3.42	4.19
	NM	5.36	3.43	3.25
US-PP (GGA)[(a)]	AFM	—	3.65	0.95
US-PP (LSDA)	NM	—	3.43	3.10
LMTO (GGA)[(b)]	—	—	3.61	2.81
LMTO (LSDA)	—	—	3.49	3.14
EXP.	AFM	2.92[(c)]	3.73	1.31

(a) Ref. [67]
(b) Ref. [68]
(c) Ref. [69], value was obtained by extrapolation of high-temperature data to room temperature.

pronounced than for the non-magnetic phases.

(III) The lattice parameter for both GGA and LSDA is smaller than experimental value, but the discrepancy between theory and experiment is reduced in GGA.

(IV) The compressibility [3], which is the reciprocal of the bulk modulus, is overestimated in LSDA. This leads to a shorter bondlength and stronger bonding compared to GGA. Therefore the cohesive energy in LSDA is also larger than in GGA.

Table 3.3 shows that the full-potential LSDA calculations are in good agreement with ultrasoft-pseudopotential (US-PP) [67] and linear-muffin-tin-orbital (LMTO) [68] calculations. All methods using GGA calculations show a thermodynamically stable AFM phase for bulk Mn.

[3] The compressibility is defined as the inverse of bulk modulus: $\kappa = \frac{1}{B_0}$.

3.3.2 Magnetic Properties

The dependence of the FM and AFM states on the volume are shown in Fig. 3.4. A high-spin state at the expanded volume is found for each of these magnetic phases and the magnetic moment is underestimated in both calculations. In the GGA calculations, the magnetic moment for the AFM state at equilibrium volume is as large as 1.9 μ_B but its value is quenched to almost zero for the FM state. The LSDA predicts the non-magnetic states as the ground state at the equilibrium volume. All in all, LSDA poorly describes the magnetization at the equilibrium volume and fails to give the experimental magnetic moment of the fcc-γ structure, which is about 2.3 μ_B .

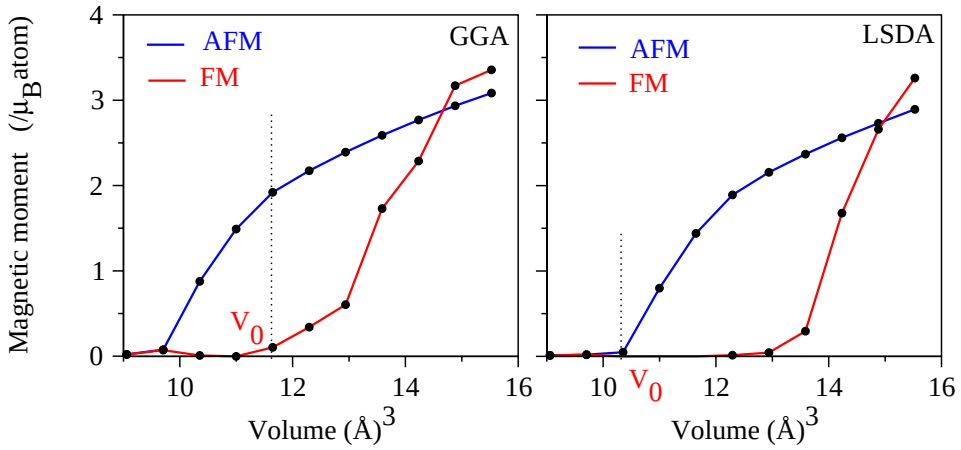

Fig. 3.4: Magnetic moment in ferromagnetic (red lines) and antiferromagnetic (blue lines) states from GGA (a) and LSDA (b) calculations.

3.4 Manganese-Silicide Compounds

Studies of Mn covered Si substrates show that Mn has the tendency to form manganese-silicide alloys on the surface [15, 16]. Our studies of the growth process of manganese on Si show that the strong covalent bond between Mn and Si lead to the formation of islands or films of Mn-Si on the Si surfaces. This makes it essential to first study the properties of some Mn-Si compounds, before turning to the films. In this chapter, the structural, magnetic and electronic properties of MnSi which could form on Si are studied (The bulk properties of Mn_3Si will be discussed in Appendix B).

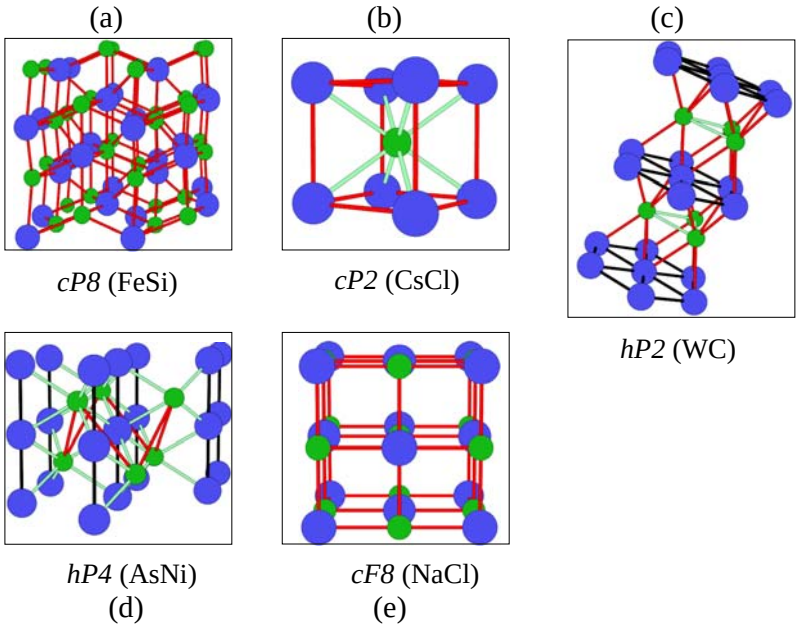

Fig. 3.5: Possible epitaxial structures of 1:1 stoichiometry of MnSi. The natural phase has FeSi structure (a) which is called B20 structure. The B2 struture (b), is the second lowest structure. The tungsten carbid, nickel arsenic and rocksalt structure are other possible epitaxial structures.

3.4.1 Bulk MnSi

Manganese mono-silicide is a magnetic intermetallic compound with B20 structure that is isostructural to non-magnetic transition metal silicides like FeSi, CoSi and CrSi. It contains four Mn and four Si atoms in a simple cubic structure with Pearson symbol $cP8$ and a lattice parameter of a_0 = 4.558 Å [70]. Mattheiss et al. [71] described the B20 structure as a rocksalt structure containing four MnSi in the unit cell where the atoms are displaced along the [111] direction. This distortion eliminates the inversion symmetry and changes the space group from $Fm3m$ to $P2_13$ [71]. The position of four Mn or Si in the unit cell are (u, u, u), ($\frac{1}{2}$ + u, $\frac{1}{2}$ - u, -u), (-u, $\frac{1}{2}$ + u, $\frac{1}{2}$ - u) and ($\frac{1}{2}$ - u, -u, $\frac{1}{2}$ + u) where u_{Mn} = 0.137 and u_{Si} = 0.845 [72]. Mn is coordinated to one Si at 2.11 Å along [111] direction, three Si neighbors at a distance of 2.35 Å and three neighbors at 2.69 Å. In the absence of a magnetic field and below T_c = 29 K, it has a helical magnetic structure with a long spiral period of 180 Å [72]. The lack of inversion symmetry is the reason of the spiral magnetic structure in the B20 crystal structure [73]. At the temperature of zero K, there is a spontaneous magnetic moment of 0.4 μ_B per Mn atom which forms a conical order phase in the magnetic field of 0.1 T [74]. The spins align as a ferromagnetic structure at 0.6 T external magnetic field [72]. The temperature increases spin fluctuation of Mn, which is called ther-

mal excitations of spin fluctuations (SFs). This induces a large magnetic moment of 2.2 μ_B [73]. The Curie temperature drops with pressure until the magnetic ordering disappears at the pressure of 1.46 GPa [75].

The growth of some mono-silicide compounds on Si substrates introduces new crystal structures which do not exist in bulk form [76]. They are formed by epitaxy and cannot be reached by external changes in pressure or temperature of bulk phase. The epitaxial stabilization of CsCl-structure of FeSi and CoSi was first observed in Si(111) surface [76].

In the following, the energy-volume curves of the epitaxial structures are compared which might conceivably form on the Si surface. In particular, the CsCl, WC, AsNi and NaCl crystal structures, Fig. 3.5, are considered which are the starting point of the forthcoming surface calculations. The optimized volume and other primitive structural properties are determined using both GGA and LSDA functionals, an energy cutoff E_{cut} =13.8 Ry and 12×12×12 k-points in the Brillouin zone.

- Structural, Electronic and Magnetic Properties

To assess the stability of various phases of manganese mono-silicide compound, the energy vs. volume curves are calculated for each structure. The curves for each structure, fitted using the Murnaghan equation, are shown in Fig. 3.6. These curves show that the stable phase is the simple cubic lattice with 4 Mn and 4 Si which corresponds to the previously mentioned B20 (or $P2_13$) structure. The calculated lattice parameter is 0.9 % smaller than the experimental value and the calculated Mn-Si bond lengths are 2.28 Å , 2.37 Å and 2.52 Å. The structural properties for all calculated phases are collected in Tab. 3.4. A FM ordering with a magnetic moment of more than 1.0 μ_B per atom is predicted for the $P2_13$ structure, which is larger than the experimental value. However, this is comparable to previous calculations done by Jeong et al. using the full-potential nonorthogonal local orbital (FP-LO) method [77].

The density of states of MnSi in Fig. 3.8-a shows metallic behavior for both spin channels. For the majority spin channel there is a narrow gap of about 0.2 eV above the Fermi level. An indirect narrow gap was also reported by Nakanishi et al [78] for the iso-structure alloy FeSi. Due to four more valence electrons per unit cell in this latter structure, its Fermi level lies in the gap, i.e. it is a normal semiconductor.

The CsCl or B2 structure appears in the regimes of high pressure. The calculations with GGA (LDA) show a phase transition from B20 structure to B2 structure at the pressure of 45 (22) GPa. This pressure is larger than the quantum critical pressure where the magnetism vanishes. Therefore it is not surprising to find the cubic B2

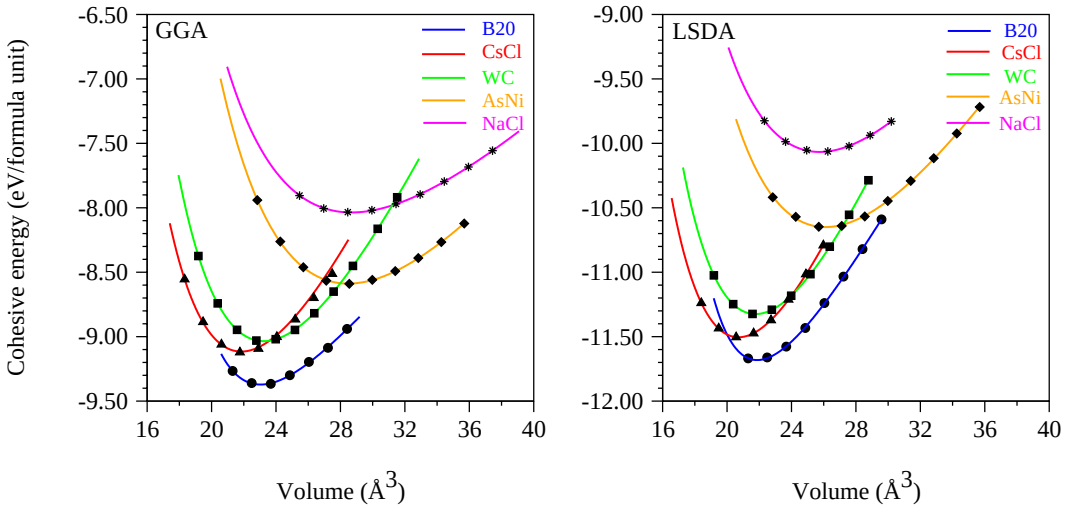

Fig. 3.6: Energy-volume curves for different epitaxy structures of MnSi are shown in the plot above. The FeSi (blue line), the CsCl (red line) and the NiAs (brown line) structures are stable in equilibrium, compressed and expanded volume, respectively. The WC (green line) and NaCl (purple line) structures are unstable.

structure with a non-magnetic phase. This structure undergoes to ferromagnetic order in a tetragonal cell. The ferromagentic structure is found upon a small distortion of the lattice, leading to an elongation of 5 % in the c direction. The calculated magnetic moment is about 0.7 μ_{B} in this tetragonal structure, the exchange splitting due to magnetization is 0.35 eV and the spinpolarization at the Fermi level is around 37 % [4]. The density of states for cubic and tetragonal structure are compared in Fig. 3.7. A difference of 0.25 eV between the cohesive energy of the B2 and the B20 structures is found, which is smaller than similar results for FeSi (0.54 eV) and CoSi (0.75 eV) [76].

The WC structure is not stable structure according to the energy-volume plot, c.f. Fig. 3.6. The lattice parameters in a and b directions are just 0.15 % shorter than in the B20 structure but an elongation of almost 20 % in the c direction is found. The space group of the tungsten carbide structure is $P\bar{6}\mathrm{m}2$; it is an hcp structure (i.e. ABAB... stacking) with Mn at (0, 0, 0) and Si ($\frac{2}{3}$, $\frac{1}{3}$, $\frac{1}{2}$), c.f. Fig. 3.5. The magnetic moment is 1.5 μ_B and the polarization at the Fermi level is about 13 %.

The AsNi structure is a metastable structure which exists in the expanded volume of 35 % compared to the equilibrium volume of the $P2_13$ structure. It has the space group $P6_3mmc$ and hexagonal structure with four basis atoms at (0,0,0) and (0, 0, $\frac{1}{2}$) for Mn and ($\frac{1}{3}$, $\frac{2}{3}$, $\frac{1}{4}$) and ($\frac{2}{3}$, $\frac{1}{3}$, $\frac{3}{4}$) for Si. The stacking is ABACABAC... with Mn in A site and Si in B and C sites. The environment of Mn atom is fcc-like and environment of Si atom is hcp-like. The cohesive energy is 0.4 eV / atom less than cohesive

[4] spin polarization at Fermi level is defined as : $(n_f^{\uparrow} - n_f^{\downarrow})/(n_f^{\uparrow} + n_f^{\downarrow})$.

Table 3.4: Lattice parameter (a_0), formation enthalpy (ΔH), bulk modulus (B_0) and magnetic moment (m) for all epitaxial structures as calculated with both GGA and LDA functionals.

	structure	a_0 Å	ΔH eV / formula unit	B_0 Mbar	m μ_B / atom
	MnSi	4.517	0.879	2.00	0.26
	CsCl	4.437	0.623	2.23	0.0
(GGA)	WC	4.524	0.542	1.19	1.5
	AsNi	4.483	0.077	2.06	1.5
	NaCl	4.859	-0.457	0.92	0.0
	MnSi	4.439	6.522	2.94	0.26
	CsCl	4.359	6.345	2.61	0.0
(LSDA)	WC	4.410	5.500	1.46	1.7
	AsNi	4.197	6.165	2.44	1.6
	NaCl	4.687	-4.907	1.30	0.0
EXP*.	MnSi	4.558			0.4

($*$) Ref. [78]

energy of B20 structure and the manganese atoms have AFM spin alignment with a magnetic moment of 1.5 μ_B. The magnetic moment in this structure and the WC crystal structure can be attributed to a distortion of cubic cell to tetragonal cell.

The NaCl structure is considered as an undistorted variant of the B20 structure [79]. This non magnetic structure is energetically unstable with a cohesive energy of almost 1.4 eV per formula unit higher than in the B20 structure. This structure has the largest equilibrium volume and compressibility of all considered structures.

Due to the deviation of the atomic positions from the structure with O_h symmetry, the B20 structure has magnetic order with a considerable magnetic moment.

In the following calculations, due to the second highest stability (after the natural B20 phase) of the B2 structure, the magnetic properties of the B2 structure will be compared with the B20 structure.

- Curie Temperature

A good magnetic material, in addition to a high magnetization, should have a high Curie temperature. In order to estimate the Curie temperature of the B2 structure, two simplest models are considered:
(i) Mohn-Wohlfarth approach:

This model is based on band theories of magnetism (the Stoner model). The features of this model are that it has a good description for the itinerant electrons, involves spin fluctuation and introduces an exchange energy which is proportional to the magnetization [80,81]. The constant of proportionality is the so-called Stoner parameter [5].
(ii) Heisenberg approach: This model usually is used for the systems with well-localized electrons.

Mohn-Wohlfarth approach: The MnSi is considered to be in the group of weak itinerant-electron ferromagnetism because of [83]:

I) a low saturation magnetic moment at the temperature of zero K (0.4 μ_{B} / Mn) [74].

II) a low magnetic order-disorder phase transition temperature ($T_C \sim$ 29K) [72].

Since MnSi is an itinerant ferromagnet, the existence of magnetism could be evaluated by the Stoner criterion [84] which states:

$$I \cdot N(\epsilon_F) > 1 \quad , \tag{3.7}$$

where I is the Stoner parameter and $N(\epsilon_F)$ is the density of states at the Fermi level in the non-magnetic phase.

The Stoner parameter is obtained from the following definition:

$$\Delta_{ex} = Im \quad , \tag{3.8}$$

where Δ_{ex}, the exchange splitting, is the band splitting between spin up and spin down channel due to magnetization. The exchange splitting is calculated directly from the total DOS of the B20 structure. m is the total magnetic moment per atom. The calculated Δ_{ex} = 0.55 eV and m = 1.0 μ_{B} yield a Stoner parameter of I = 0.5 eV / μ_{B}.

From the Stoner model, the magnetic phase appears when the gain in the exchange energy is larger than the loss in kinetic energy. Additionally, this model allows us to understand the structural dependence of the magnetic moment in the structures. This dependency is explained by comparing the DOS of the B2 and the B20 structures (Fig. 3.7 and 3.8) :
The non-magnetic B20 DOS has several peaks which belong to itinerant electrons. The Fermi level in MnSi DOS lies on one of the peaks which results in a higher density of states than for the cubic B2 structure. On the other hand in the cubic B2 DOS

[5] The Stoner parameter is an intra-atomic quantity that does not depend on the crystal environment and structure [82].

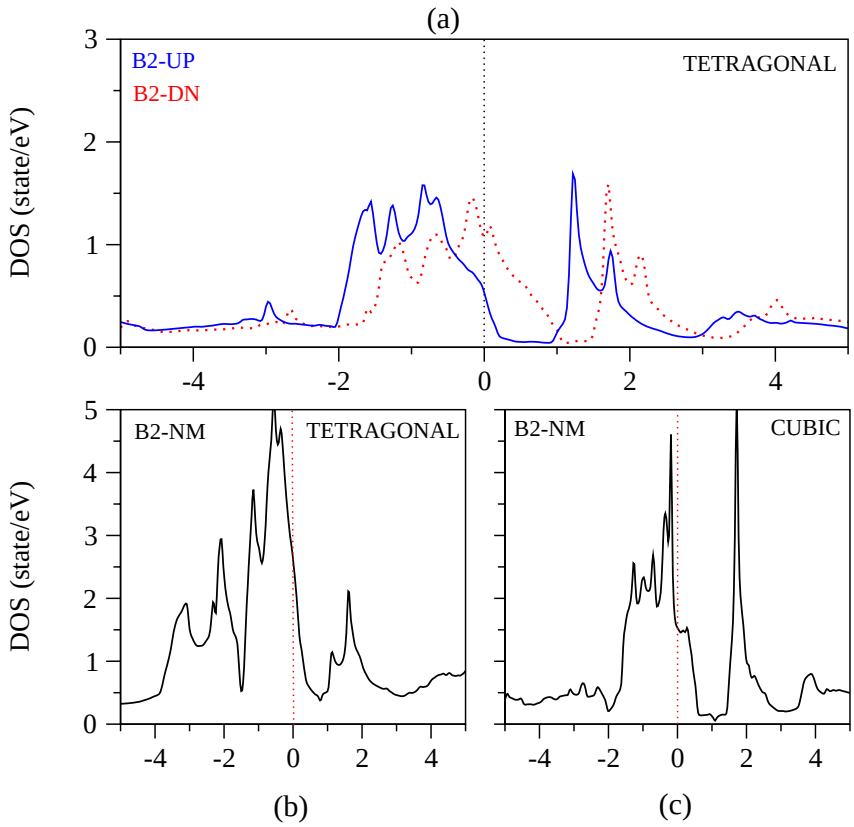

Fig. 3.7: Density of states (N) for MnSi in the B2 structure using a ($12 \times 12 \times 12$) k-point grid in the Brillouin-Zone. The filled blue (red dash) line is the DOS for the B2 in the majority (minority) spin channel (a). The black line is the DOS of the non-magnetic phase for both spin channels (b, c). The Fermi level is taken as the energy zero.

the Fermi level is in the shoulder of the peak, c.f. Fig. 3.8. In the DOS of the cubic B2 structure, there are several occupied peaks for the t_{2g} band and one peak which has e_g character. The Fermi level is in the shoulder of the lower peak which results in a low density of states at the Fermi level ($\sim$ 1.5 state / eV), see Fig. 3.7-c. As the Stoner parameter is the same for both structures [82], the Stoner criterion is fulfilled for B20 but not for the cubic B2 structure. These results are in agreement with the thermodynamical stability of the non-magnetic phase of the B2 cubic structure and the magnetic ground state order of the B20 structure. However, with distortion of the B2 structure in c direction (at constant volume), one can get a magnetic structure [85]. In the present work with the lattice distortion of 5 % in c direction, we get a magnetic moment of 0.7 μ_B / Mn atom. The density of states for cubic and tetragonal structure in non-magnetic and magnetic order are shown in Fig. 3.7-b, c. The density of states at the Fermi level in the non-magnetic cubic B2 structure is about 1.5 state / eV but rises up to 2.6 state / eV in the tetragonal structure, c.f. Fig. 3.7-b, c and leads to satisfy the Stoner criterion.

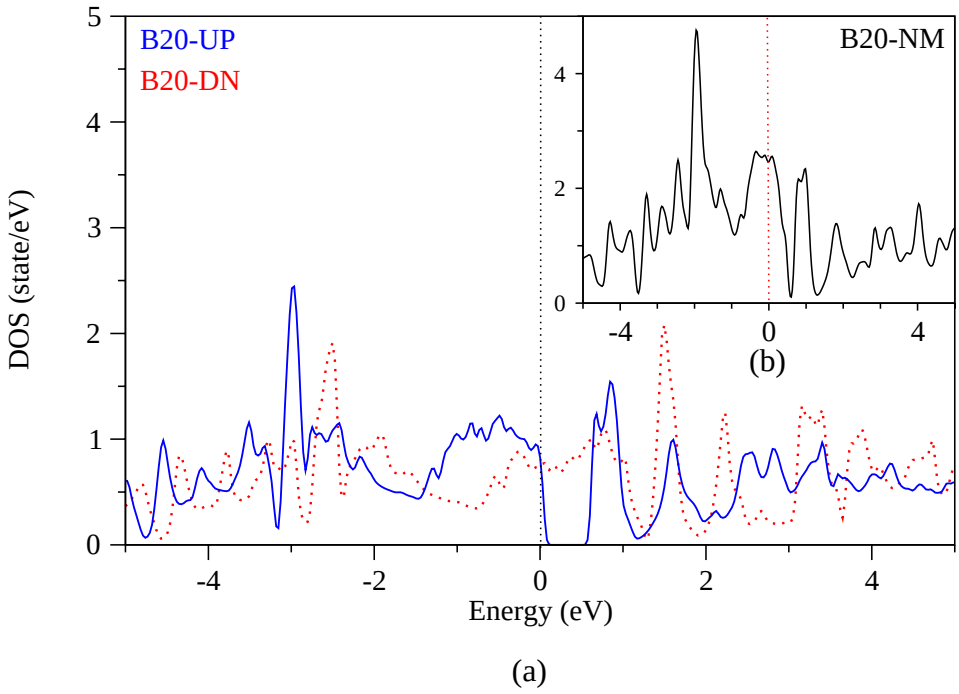

Fig. 3.8: Density of states (N) for MnSi in the B20 structure using a ($12 \times 12 \times 12$) k-point in the Brillouin-Zone. The blue filled (red dash)line is the DOS of the majority (minority) spin channel (a). The black line is the DOS of the B20 structure in the non-magnetic phase for both spin channels (b). The Fermi level is referred to the energy zero level.

The simplest approach to estimate the Curie temperature of itinerant magnets is to consider Stoner excitations. The Stoner excitations lead to a reduced magnetic moment with raising the temperature, which finally vanishes at $T = T_C$. The Curie temperature from the Stoner model, T_S, is defined as [81] :

$$I(\epsilon_F) \int_{-\infty}^{\infty} \frac{\partial f(\epsilon, T)}{\partial \epsilon} \, n_{\mathrm{nm}}(\epsilon) \, d\epsilon + 1 = 0 \qquad . \tag{3.9}$$

where $n_{\mathrm{nm}}(\epsilon) = 1/2 \; N_{nm}(\epsilon)$ is the density of states per atom and spin in the non-magnetic state, and $f(\epsilon, T)$ is the Fermi distribution function which is a function of temperature. The solution of above equation gives the Stoner temperature (T_S).

However, the Stoner model yields a Curie temperature that is too high. There is the semiempirical approach developed by Mohn and Wohlfarth [80] which calculates the Curie temperature of a very weak itinerant ferromagnet involving spin fluctuations [86] . In this approach, long-wavelength spin fluctuations are made responsible for the Curie temperature.

Table 3.5: Density of states per Mn at the Fermi level for both spin channels ($n_\uparrow(\epsilon_F)$, $n_\downarrow(\epsilon_F)$), total density of states at the Fermi level for the non-magnetic case ($n_{nm}(\epsilon_f)$), the exchange splitting (Δ_{ex}), the magnetic moment m, the Stoner parameter (I), the Pauli susceptibility (χ) and the Curie temperature (T_C) calculated by Mohn-Wohlfarth theory.

	$n_\uparrow(\epsilon_F)$	$n_\downarrow(\epsilon_F)$	$N_{nm}(\epsilon_F)$	Δ_{ex} (eV)	m (μ_B)	I (eV / μ_B)	χ	T_C^{SF} (K)
B20	0.5	0.6	2.5	0.52	1.0	0.5	1.6	609
B2	0.6	1.2	2.6	0.35	0.7	0.5	2.7	225

This theory contains three parameters: saturation magnetization, Pauli susceptibility and Stoner parameter. Despite its theoretical shortcomings, this approach has been widely used to evaluate experimental data on intermetallic materials.

In the Mohn-Wohlfarth theory the mentioned parameters are related in this formula

$$\frac{T_C^2}{T_S^2} + \frac{T_C}{T_{SF}} = 1 \qquad , \tag{3.10}$$

where T_S is the Stoner-model Curie temperature, and the spin-fluctuation temperature T_{SF} is given by:

$$T_{SF} = \frac{m^2}{20 k_B \chi_0} \qquad , \tag{3.11}$$

where χ_0 is the spin susceptibility at equilibrium and m is the averaged magnetic moment per Mn (in units of μ_B).

$$\chi_0^{-1} = (1/2\mu_B^2)(\frac{1}{2n_\uparrow(\epsilon_F)} + \frac{1}{2n_\downarrow(\epsilon_F)} - I) \qquad . \tag{3.12}$$

Here $n_\uparrow(\epsilon_F)$ and $n_\downarrow(\epsilon_F)$ are the zero-temperature densities of states per atom at the Fermi level of the spin up and down bands, and I is the Stoner parameter. Often the Stoner temperature, T_S is much higher than the spin fluctuation temperature T_{SF}; therefore, the Curie temperature is estimated just by T_{SF} ($T_C \sim T_{SF}$) .

The density of states at the Fermi level, the exchange splitting energy, the Stoner parameter, the Pauli susceptibility and finally the Curie temperature for both B2 and B20 structures are summarized in Tab. 3.5. As one sees, this approach still yields a

very high Curie temperature for both structures.

Heisenberg approach: In this approach, the Curie temperature is calculated from the total energy difference of the ferromagnetic and the antiferromagnetic state in the nearest-neighbor Heisenberg model [87]. Here, one starts with the Heisenberg Hamiltonian

$$H = -J \sum_i \sum_j \mathbf{S}_i \mathbf{S}_j \quad . \tag{3.13}$$

which describes the isotropic exchange interaction, J, between the spins located on a three-dimensional lattice. It is assumed that the exchange interaction between nearest-neighbor atoms is the dominant one, thus the summation runs over all nearest-neighbor sites.

The Curie temperature of the Heisenberg ferromagnet in the mean-field approximation is described in Ref. [88]:

$$T_C^{MF} = 2J \frac{\gamma}{3K_B} = 2 \frac{E_{\mathrm{AFM}} - E_{\mathrm{FM}}}{3k_B} \quad . \tag{3.14}$$

Table 3.6: Energy difference in DFT-GGA between FM and AFM order per formula unit and calculated Curie temperature for B20 and B2 structures.

	$E_{\mathrm{AFM}} - E_{\mathrm{FM}}$ (meV)	T_C (K)
B20	11	85
B2	11	85

The factor γ is given by $S(S+1)/S^2$ for quantum spins and it equals to 1 for classical spins, E_{AFM} and E_{FM} are the energy of antiferromagnetic and ferromagnetic structures. Choosing the empirical value of $\gamma = 1$ leads to a good agreement with the experiment [88].

The energy of ferromagnetic and antiferromagnetic order and the calculated Curie temperature in the Heisenberg model are summarized in Tab 3.6. The Heisenberg model predicts the Curie temperature more realistic than the Stoner model, and shows low Curie temperature (below room temperature) for bulk structures of Mn-mono-silicide.